Journal of Photochemistry & Photobiology, B: Biology 250 (2024) 112832

Contents lists available at ScienceDirect

Journal of Photochemistry & Photobiology, B: Biology

journal homepage: www.elsevier.com/locate/jphotobiol

Cyclometalated Ir(III) theranostic molecular probe enabled mitochondria targeted fluorescence-SERS-guided phototherapy in breast cancer cells

Chandana Reghukumar [a,b], Shanmughan Shamjith [a,b], Vishnu Priya Murali [a], Pilankatta K. Ramya [a,b], Kokkuvayil Vasu Radhakrishnan [a,b], Kaustabh Kumar Maiti [a,b,*]

[a] Chemical Sciences & Technology Division (CSTD), Organic Chemistry Section, CSIR-National Institute for Interdisciplinary Science & Technology (CSIR-NIIST), Industrial Estate, Pappanamcode, Thiruvananthapuram 695019, Kerala, India
[b] Academy of Scientific and Innovative Research (AcSIR), Ghaziabad 201002, India

ARTICLE INFO

Keywords:
Mitochondria targeting
Photodynamic therapy
Iridium complex
Reactive oxygen species
Cancer theranostics
SERS

ABSTRACT

The increased energy demands inherent in cancer cells necessitate a dependence on mitochondrial assistance for their proliferation and metastatic activity. Herein, an innovative photo-medical approach has been attempted, specifically targeting mitochondria, the cellular powerhouses, to attain therapeutic benefit. This strategy facilitates the rapid and precise initiation of apoptosis, the programmed cell death process. In this goal, we have synthesized cyclometalated Iridium (III) molecular probes, denoted as Ir-CN and Ir-H, with a nitrile (CN) and a hydrogen-functionalized bipyridine as ancillary ligands, respectively. Ir-CN has shown superior photosensitizing properties and lower dark cytotoxicity compared to Ir-H in the breast cancer cell line MCF-7, positioning it as the preferred probe for photodynamic therapy (PDT). The synthesized Ir-CN induces alterations in mitochondrial membrane potential, disrupting the respiratory chain function, and generating reactive oxygen species that activate signaling pathways leading to cell death. The CN-conjugated bipyridine ligand in Ir-CN contributes to the intense red fluorescence and the positive charge on the central metal atom facilitates specific mitochondrial colocalization (colocalization coefficient of 0.90). Together with this, the Iridium metal, with strong spin-orbit coupling, efficiently generates singlet oxygen with a quantum yield of 0.79. Consequently, the cytotoxic singlet oxygen produced by Ir-CN upon laser exposure disrupts mitochondrial processes, arresting the electron transport chain and energy production, ultimately leading to programmed cell death. This mitochondrial imbalance and apoptotic induction were dually confirmed through various apoptotic assays including Annexin V staining and by mapping the molecular level changes through surface-enhanced Raman spectroscopy (SERS). Therefore, cyclometalated Ir-CN emerges as a promising molecular probe for cancer theranostics, inducing laser-assisted mitochondrial damage, as tracked through bimodal fluorescence and SERS.

1. Introduction

According to WHO data, cancer accounts for one in six leading causes of death worldwide and is the second biggest cause of mortality [1,2]. Over time, there has been a sharp rise in the incidence of cancer, which is still a hazard. Cancer is the term used to describe the unchecked proliferation of cells, often resistant to the anti-growth mechanism [3]. These cancer cells can multiply, evade apoptosis, create new blood vessels, and spread throughout the body. Due to its adverse side effects, drug resistance, and non-targeted action, chemotherapy, the traditional medication-based treatment, was often unsuccessful in a majority of instances [4]. Subsequently, as an alternative anti-cancer therapy, photodynamic therapy (PDT) is being utilized in certain cancer treatments which is a light-based technology that has benefits over conventional cancer therapies for solid tumors [5].

PDT has a superior treatment option to traditional cancer treatment modalities as an individualized precision treatment by its precise controllability and minimal/non-invasiveness [6]. PDT is the result of the interaction of three key components: a photosensitizer (PS), light with a certain wavelength, and the presence of molecular oxygen [7]. The photosensitizer absorbs light when exposed to the target tissue, which sets off a cascade of photochemical events that lead to the

* Corresponding author at: Chemical Sciences & Technology Division (CSTD), Organic Chemistry Section, CSIR-National Institute for Interdisciplinary Science & Technology (CSIR-NIIST), Industrial Estate, Pappanamcode, Thiruvananthapuram 695019, Kerala, India.
E-mail address: kkmaiti@niist.res.in (K.K. Maiti).

https://doi.org/10.1016/j.jphotobiol.2023.112832
Received 9 October 2023; Received in revised form 8 December 2023; Accepted 15 December 2023
Available online 21 December 2023

production of ROS [8]. To achieve the desired therapeutic effect, a variety of factors should be considered when standardizing the treatment protocol, including the type of PS used, the dose administered, the intracellular location of the PS upon internalization, the drug-to-light interval (DL1), the total amount of light applied, its wavelength, and fluence rate, the characteristics of the tumor, and the local availability of oxygen [6,9,10].

Considering the therapeutic outcome of cisplatin, other transition metal complexes have been investigated as anti-cancer agents by redesigning by ligand substitution on existing chemical structures or by synthesizing an entirely new chemical entity [11,12]. Likewise, the usage of metal complexes as photosensitizers for PDT has dramatically increased over the past decade [13]. The fact that the metal complexes satisfy several crucial parameters for a photosensitizer is the cause of their increasing popularity. The heavy atom promotes spin-orbit coupling, leading to a population of efficient and ultrafast triplet-excited states [14,15]. In general, high yields of triplet excited states lead to high yields of singlet oxygen generation. Nonetheless, due to their prolonged emission lifetimes, metal complexes are sensitive to the intracellular milieu, making them potential "see and cure" agents [16]. Metal complexes are typically photostable under sustained one- and two-photon illumination, in contrast to the majority of colored organic compounds. This allows for the longer recycling of the PS and, as a result, a reduction in the overall dose of PS required [17]. The relative ease with which metal complexes can be created, where various ligands and metal centers can be coupled in an almost combinatorial fashion, adding to these desirable photophysical properties, provides the chance to modify those features as needed [18].

In the scenario of intracellular metabolic events, mitochondria serve as both the location of eukaryotic oxidative metabolism and the source of energy as reflected in the production of ATP [19]. The tricarboxylic acid cycle and oxidative phosphorylation, which correspond to the second and third stages of aerobic respiration, are used to characterize the common mechanism of mitochondrial oxidation [20]. Contrarily, mitochondria are essential for controlling intrinsic apoptosis. The intermembrane space (IMS) of mitochondria releases proproteins of apoptosis to the cytosol in the normal apoptotic route [21]. The ability of cancer cells to switch between glycolysis and oxidative phosphorylation has been found to have a role in providing resistance towards oncogene inhibition [22,23]. Since it was also discovered that mitochondria play a significant role in controlling cell death, mitochondria-targeted photodynamic therapy (Mt-PDT) was developed as a promising strategy for eliminating cancer cells [21,24]. Many mitochondrial targeting molecular PSs are reported using lipophilic cations in line with the overall mitochondrial transmembrane potential (MTP) [25]. In general, cyclometalated Ir (III) complexes are well-known examples of mitochondrial localization due to their inherent positive charge on the metal, making it an ideal Mito-targeted PDT agent [26,27]. Considering all these facts, we hypothesized that cyclometalated Iridium (III) complexes can be utilized as efficient molecular probes for creating new luminous PDT agents.

Considering this in mind, we have demonstrated a comprehensive exploration encompassing the design, synthesis, and meticulous optimization of two distinct cyclometalated Iridium complexes, denoted as Ir-CN and Ir-H, both of which exhibit remarkable pH stability and photostability. Our investigation extends to the characterization of these complexes, unveiling their potential as photosensitizers in various applications. The rigorous scrutiny of the photophysical properties and comprehensive toxicity profiling underscores the clear superiority of Ir-CN over Ir-H. This observation renders Ir-CN an exceptionally promising candidate for further in-depth in vitro assessment. Remarkably, Ir-CN demonstrates swift internalization into cancer cells, achieving localization within mitochondria in a time frame of less than one hour. Furthermore, it exerts significant antitumor activity when subjected to laser irradiation, primarily through the activation of apoptotic pathways driven by an abnormal amplification of reactive oxygen species (ROS). The exclusive capacity of Ir-CN to generate singlet oxygen upon laser irradiation endows it with an ideal profile for precision therapy. Beyond its phototherapeutic potential, Ir-CN boasts a dual functionality as a two-in-one bimodal probe. The inherent red fluorescence and the distinct Raman peak associated with the CN moiety enable its utility in mitochondria-targeted image-guided photodynamic therapeutic assessment. This as-mentioned approach leverages bimodal fluorescence and Raman spectroscopy for precise monitoring of the therapeutic progression, highlighting the multifaceted utility of Ir-CN in scientific research and potential clinical applications. (Scheme 1).

2. Results and Discussion

2.1. Design, Synthesis, and Characterization of the Cyclometalated Ir(III) Complexes

Cyclometalated Iridium (III) complexes, Ir-CN and Ir-H, were synthesized through a multi-step procedure. Initially, a chlorine-bridged dimeric Iridium complex was formed by employing the Nonoyama reaction, which involved the reaction between $IrCl_3{\cdot}3H_2O$ and 2-phenylpyridine. Subsequently, ancillary ligands, namely 4,4′-([2,2′-bipyridine]-4,4′-diyl) dibenzonitrile (for Ir-CN) and 4,4′-diphenyl 2,2′-bipyridine (for Ir-H), were synthesized via a palladium-catalyzed Suzuki cross-coupling reaction [28]. Finally, the chlorine bridges were replaced with bipyridine ligands, yielding Ir-CN and Ir-H as solid compounds with orange and pale orange colors, respectively. To substitute the chlorine counter ions in the complexes with hexafluorophosphate anions, the anion exchange reaction was carried out using potassium hexafluorophosphate. Comprehensive characterization of the prepared cyclometalated iridium complexes Ir-CN, Ir-H, and their intermediates was accomplished using advanced spectroscopic techniques, including ^{1}H NMR, ^{13}C NMR, and high-resolution mass spectrometry (HRMS). (Fig. S1 to S11).

Iridium complexes exhibit a range of advantageous characteristics when employed as photosensitizing agents in Photodynamic Therapy (PDT). These complexes possess unique photophysical properties, such as prolonged excited states and efficient inter-system crossing, making them exceptionally proficient at generating reactive oxygen species when exposed to light. Moreover, their outstanding stability in biological environments and versatile chemical adaptability further enhance their suitability as PDT agents. These features hold the potential for precise and selective eradication of cancer cells while minimizing damage to healthy tissues. In both complexes, the central metal component of the cyclometalated ligand imparts a net $^{+}1$ charge to the overall complex, enhancing its specific interaction capacity with negatively polarized mitochondria, making it an excellent candidate for targeting mitochondria in PDT. The CN centers within the appended bipyridine portion of Ir-CN introduce a strong electron-withdrawing effect, resulting in an extended red emission in the compound. Additionally, the presence of a triple bond in the CN unit imparts distinct Raman fingerprints in the cell's silent region of Raman spectra, resembling a marker peak for Raman-based characterization of the probe when compared to the non-substituted counterpart Ir-H. The disparities in emission profiles and the sharp Raman peak at 2190 cm^{-1} serve as valuable distinguishing features for these molecules in both fluorescence and Raman-based platforms (Fig. 1d, e).

2.2. Energetic Assessment of Ir-CN and Ir-H

Head-Gordon and colleagues' density functional theory (DFT) technique using the wB97xD method is used for the optimization of all geometries, which integrates dispersion and has excellent geometry optimization performance. As the molecular complexes are large, the 6-31G(d) moderate size double zeta split-valence basis set with polarisation function is used for all main block elements, while the LanL2DZ basis set is used for Ir, with the inner core electrons replaced with Hay

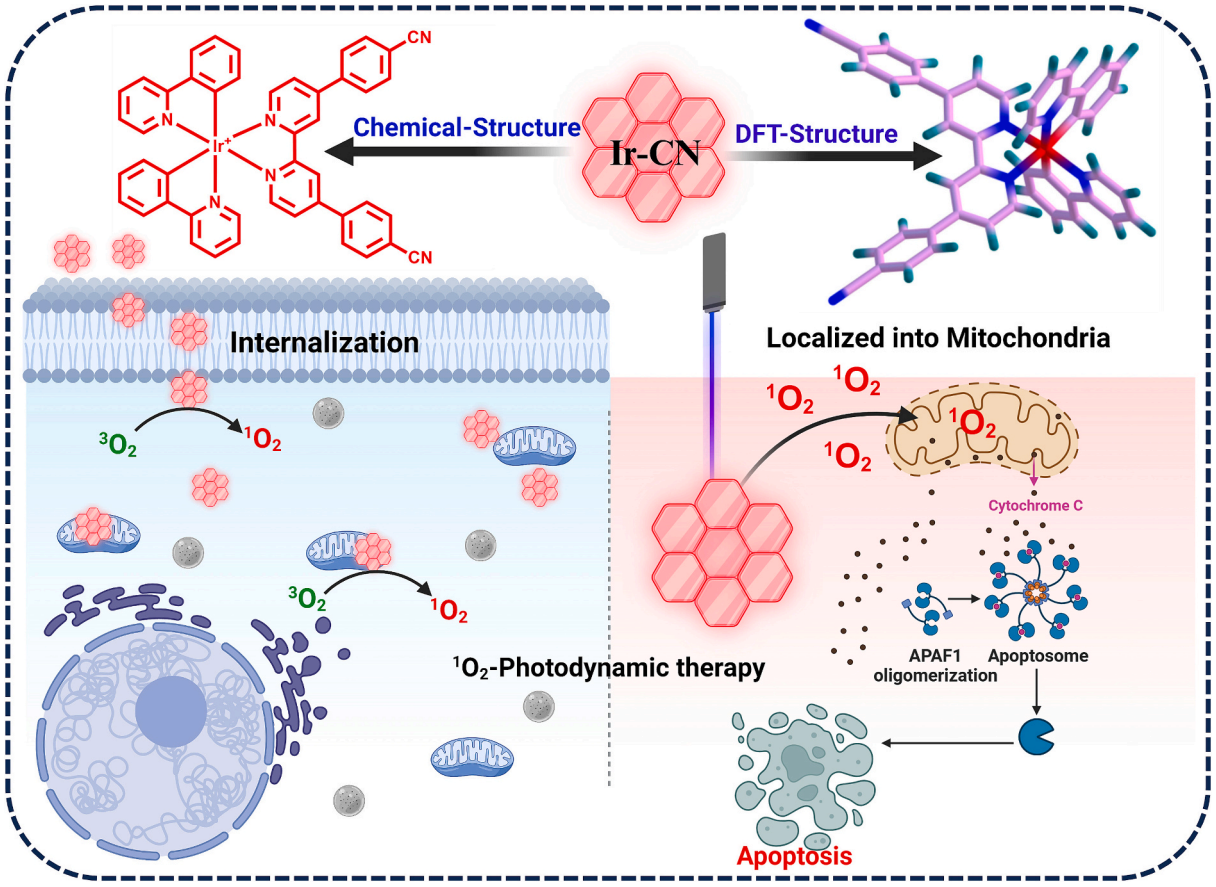

Scheme 1. Schematic illustration of mitochondrial-targeted PDT induced by Ir-CN (Created with BioRender.com). Ir-CN, the novel Ir(III) based photosensitizer, upon incubation with MCF-7 breast cancer cells, gets easily internalized to provide red fluorescence mainly from the mitochondrial region of the cells. The Ir-CN treated cells were irradiated with a laser to induce ROS generation, leading to cellular apoptosis.

and Wadts' relativistic effective core potential (ECP). This method is abbreviated as wB97xD/BS. Furthermore, at the wB97xD/BS level, vibrational frequency analysis was conducted to validate the nature of the optimized structures. The minimum of the complexes was verified by ensuring the absence of imaginary frequencies. To account for solvation effects, particularly in dimethylsulfoxide (DMSO), the optimization process incorporated the implicit self-consistent reaction field model (SCRF), specifically SMD, as implemented in Gaussian16. The band gaps (E_g) for both complexes are determined by subtracting the corresponding HOMO and LUMO energies. It is worth noting that the complex Ir-H exhibits a slightly higher E_g compared to the Ir-CN complex. The energetics of the two complexes are tabulated in Table 1.

2.3. Photophysical and Stability Evaluation of Ir-CN and Ir-H

The UV–Vis absorption of both the complexes has been measured in DMSO (10 μM at 25 °C). UV–Vis absorption spectrum of the complexes Ir-CN (10 μM in DMSO at 25 °C) showed energy absorption bands at 230–350 nm (Fig. 1c) corresponding to the spin-allowed ligand centered π-π* transitions for cyclometalated (Ppy) and ancillary ligands [29]. The mixed singlet and triplet metal-to-ligand charge transfer (^{1}MLCT and ^{3}MLCT) and ligand-to-ligand charge-transfer (LLCT) transitions are responsible for the weak and low-energy bands between 400 and 510 nm[16]. When the complexes are subjected to long UV light irradiation from a standard UV lamp, both emanate sharp red fluorescence. The complex Ir-CN exhibits a wide emission peak centered at 645 nm after being excited at 405 nm (excitation slit width 3 nm, emission slit width 3 nm) (Fig. 1c) while Ir-H showed a wide emission peak centered at 620 nm upon excitation at 385 nm (excitation slit width 3 nm, emission slit width 3 nm) (Fig. S12). Moving on to the Raman spectroscopic analysis, the complex Ir-CN shows a sharp Raman peak at 2190 cm^{-1} (Fig. 1d) corresponding to the CN vibration in bare Raman mode making it an ideal probe for intracellular investigation through Raman modality whereas the absence of this peak in the Ir-H complex clearly confirms the presence of CN. Additionally, the SERS studies of Ir-CN were carried out using spherical gold nanoparticles (AuNPs: 35–40 nm) to evaluate the surface-enhanced Raman peaks of the Ir-CN for monitoring the ultra-sensitive responses. The Raman fingerprinting of Ir-CN showed excellent Raman signals, viz., highly intense peak 2129 cm^{-1} due to the CN vibration and few sharp bands such as the one corresponding 1023 cm^{-1} due to ring breathing from the phenyl part in the complex, making them promising candidates for SERS based probes for imaging the cells through Raman platform (Fig. 1e). Utilizing pH titration at several pH levels ranging from 4.5 to 9.5 confirms the stability of Ir-CN and Ir-H absorption and emission characteristics in a range of pH environments (Fig. 1f and S14).

Assessing photostability is a critical consideration when examining photosensitizing agents for photodynamic therapy (PDT). To assess this, both the intricate Ir-CN and Ir-H complexes were subjected to exposure from a 405 nm laser over a specific duration, and their photophysical properties were thoroughly analyzed. As anticipated, both complexes exhibited remarkable stability over an extended timeframe, providing substantial evidence in favor of the photostability of these molecules (as depicted in Fig. 1g, h, S13). Furthermore, when evaluating the parameters within environments comprising 10% fetal bovine serum (FBS), phosphate-buffered saline (PBS), and pure water, we observed consistent absorption and emission intensity profiles. This once again underscores the robust and enduring nature of our complex.

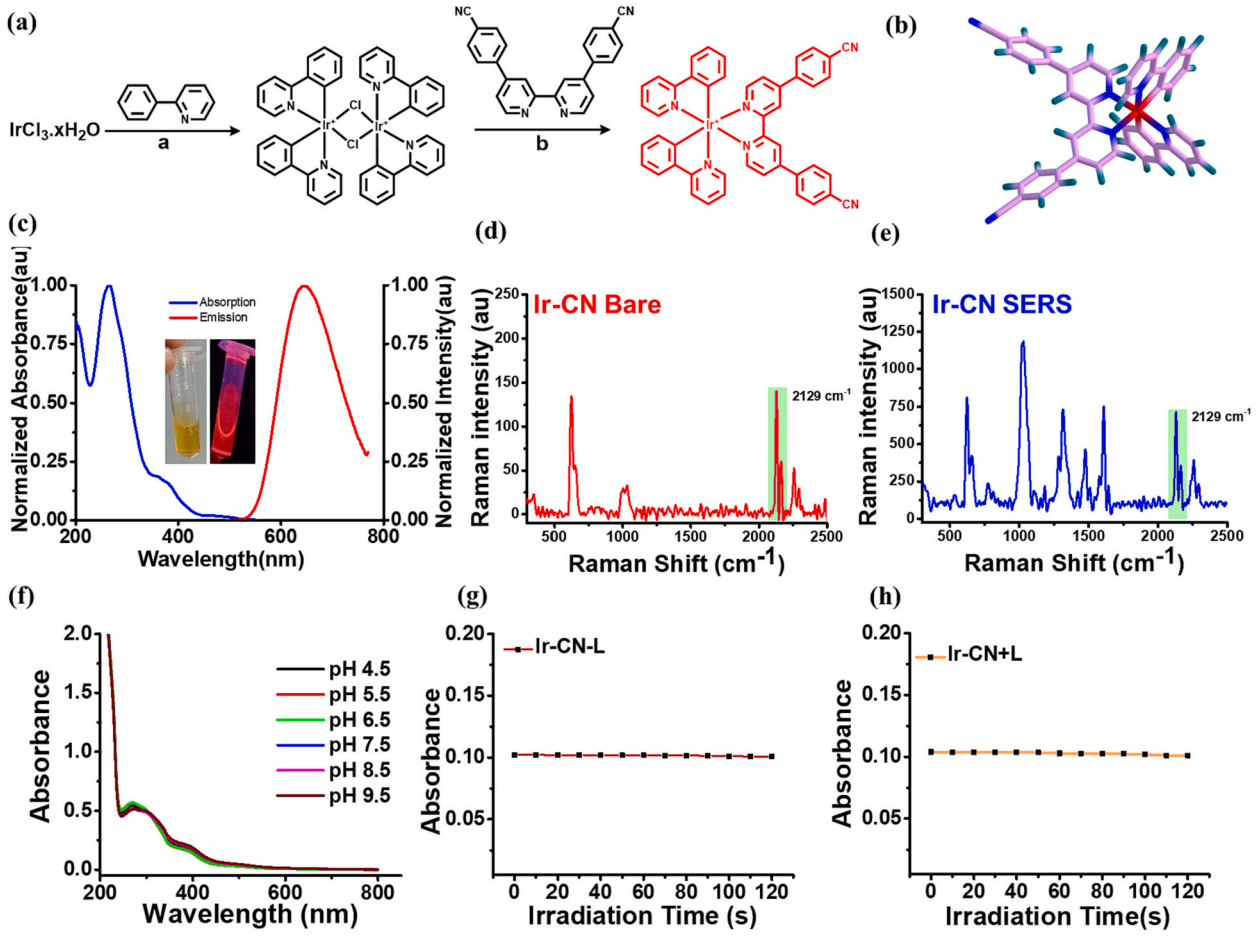

Fig. 1. (a) Schematic workflow of synthesis of Ir-CN. (b) DFT optimized structure of Ir-CN (c) UV–Vis absorbance and emission spectra of 10 μM Ir-CN in DMSO at 25 °C (d) Characteristic Raman Fingerprint of Ir-CN (e) SERS spectra of Ir-CN with spherical gold nano-particle in 1:9 ratio indicating the cell silent peak at 2129 cm^{-1} (f) Graph showing the stability of Ir-CN in varying pHs (g) Graph depicting the photostability of Ir-CN without laser and (h) with laser. (For interpretation of the references to colour in this figure legend, the reader is referred to the web version of this article.)

Table 1
The energy data (in a.u) obtained at wB97xD/SMD/BS level for the Ir-CN and Ir-H.

Molecules	SCF energy	Zero-point corrected energy	Free energy	Free energy correction	HOMO energy	LUMO energy	Band gap
	E	ZPE	G	G(corr)	E_{HOMO}	E_{LUMO}	E_g
Ir-CN	−2203.48478	−2202.83258	−2202.91028	0.574494	−0.27766	−0.02785	0.24982
Ir-H	−2019.06802	−2018.41332	−2018.48589	0.582132	−0.27652	−0.01960	0.25691

2.4. Photoactivation and Singlet Oxygen Generation of Ir-CN and Ir-H

Although, compared to organic photosensitizers, the use of metal-based complexes for phototherapy is still in its infancy, the chemical expertise gained through years of experience with cisplatin and other metal-based medications can speed up the development of photo-activatable complexes [30]. Complexes based on noble metals display PDT activity as photosensitizers due to their tunable photophysical and photochemical features and considerable ROS generation [11]. In consequence, advancements in this field open new opportunities for the use of bioinorganic chemistry in medicine. In general, because of their adjustable photophysical and photochemical properties, cyclometalated iridium complexes have recently attracted a lot of attention as potential PDT agents. It is well known that the efficiency of intersystem crossover (S1 to T1) and the subsequent energy transfer from triplet oxygen are directly correlated with $^1O_2$ generation (Fig. 2a). These generated oxygen species attack the organelles leading to apoptosis (Fig. 2b). Using the well-known $^1O_2$ scavenger dye 1,3-diphenylisobenzofuran (DPBF) (Fig. 2c) and a structurally significant molecule $[Ru(Bpy)_3]Cl_2$ as standard reference material, the Ir-CN and Ir-H were examined for their ability to generate $^1O_2$. For this, the material under investigation was mixed with oxygen scavenger DPBF in a 1:3 ratio of its absorbance. The mixture was capped well and irradiated with a 405 nm laser, later its absorption and emission profiles were measured. The molecules when darted with laser sharply attenuate the absorption of DPBF at 410 nm due to the singlet oxygen cycloaddition (Fig. 2d). Similarly, the sharp emission bands of DPBF at 450 and 500 nm were quenched effectively, which would also correlate with the singlet oxygen production (Fig. 2e). The ability of Ir-CN to generate $^1O_2$ is amply demonstrated by a decrease in the absorbance and emission profiles of DPBF within 240 s. When compared to the reference $[Ru(Bpy)_3]Cl_2$, which had a singlet oxygen quantum yield of 0.57, the Ir-CN was found to have a value of 0.79 whereas Ir-H has a value of 0.72 making Ir-CN a good candidate over Ir-H (Fig. 2f, S15).

The increased quantum yield is clearly determined by the liner plot of the change in absorbance of DPBF (ΔA) caused by Ir-CN and Ir-H with

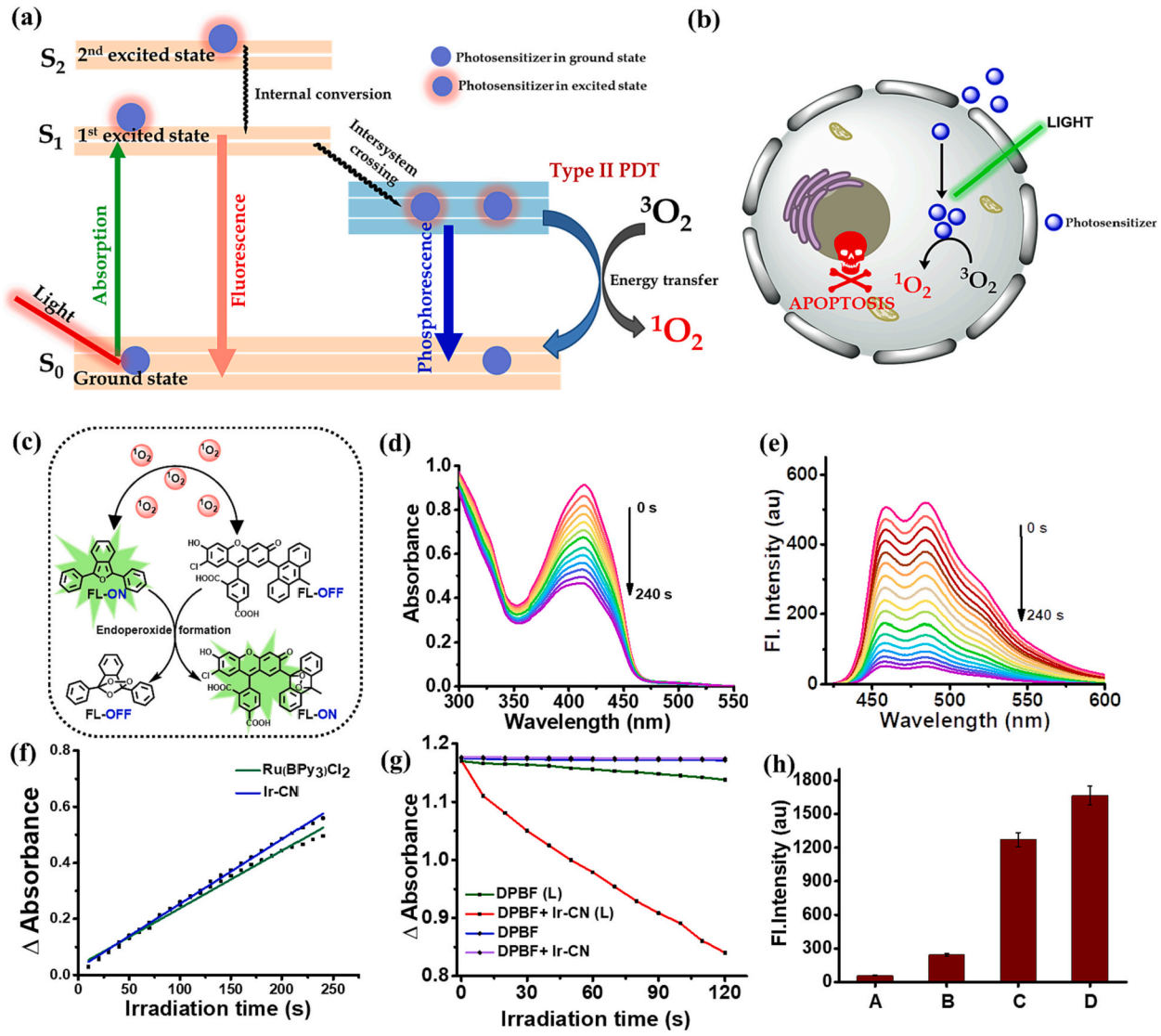

Fig. 2. (a) Schematic representation of Jablonski diagram depicting Type II photosensitization and singlet oxygen generation (b) Pictorial representation of apoptosis induced by singlet oxygen generation in cells (c) Mechanism of emission turn-off of DPBF and turn-on of SOSG during singlet oxygen cycloaddition (d) Attenuation of 410 nm peak of DPBF during photoactivation of Ir-CN (e) Emission quenching of DPBF with generated singlet oxygen during the photoactivation of Ir-CN (f) Linear plot of Ir-CN and $Ru(Bpy)_3Cl_2$ used for the calculation of singlet oxygen quantum yield (g) Relative singlet oxygen generation of Ir-CN along with other combination (h) Confirmation of singlet oxygen generation ability of Ir-CN and other combination using SOSG (A- SOSG alone, B- SOSG + Ir-CN without laser, C- SOSG+ Ir-CN with laser irradiation for 1 min, D- SOSG+ Ir-CN with laser irradiation for 2 min).

respect to time. Both DPBF alone and in different combinations are unable to have this effect. The relative singlet oxygen production calculated by the change in optical density of DPBF with various trials evidentially confirms the superiority of Ir-CN over other combinations. These sharp emission and absorption changes caused by Ir-CN with the laser to the scavenger molecule unequivocally supported Ir-CN's potential as a photosensitizer moiety (Fig. 2g). Finally, the singlet oxygen production in the solution state was further confirmed by the well-known singlet oxygen indicator Singlet Oxygen Sensor Green (SOSG). The PeT phenomenon between the anthracene subunit and the central oxygen atom in the main ring quenched the dye SOSG's emission properties. Upon interaction with the singlet state oxygen, the anthracene part underwent a cycloaddition reaction which eventually stops the PeT process and turns on the emission behavior. The dye SOSG alone and in combination with the complex Ir-CN will emit light with a relatively weak center of emission at 525 nm, but after being exposed to 405 nm laser radiation for up to two minutes, the emission profile will dramatically rise by 4 to 6 times (Fig. 2h, D). The presence of singlet oxygen during the photoirradiation process is amply confirmed by the fast regeneration of SOSG emission (Fig. 2h).

2.5. *Evaluation of Cytotoxicity and Cellular Internalization of Molecular Probe Ir-CN and Ir-H*

The assessment of cytotoxicity is a prerequisite for any molecular probe before proceeding to further studies on in vitro biological assessment. Being non-toxic to the cells in dark conditions is an imperative feature for any PDT agent, at the same time, it should be activated upon proper irradiation. MTT assay was employed to determine the dose and time-dependent cytotoxicity of Ir-CN and Ir-H in the absence of laser irradiation. The assay enables the measurement of cell viability by assessing the cleavage of tetrazolium salt by mitochondrial dehydrogenase. Initially, MCF-7, a breast cancer cell line was subjected to the treatment with both the candidate compounds. The results revealed that even at a concentration as low as 5 μM, Ir-H caused a depletion in cell viability to 60% (Fig. S23, Table S2), whereas Ir-CN does not exhibit a

significant cytotoxic effect up to 20 μM concentration within 6 h, showing 98% cell viability (Fig. S24, Table S3). As shown in Fig. S25, even after 24 h incubation, 10 μM concentration of the latter retained about 90% cell viability (Table S4).

Owing to the augmented dark cytotoxic nature, Ir-H was subsequently eliminated and Ir-CN was chosen for further studies. Furthermore, Ir-CN was also found minimal cytotoxic effect on the normal breast epithelial cell line MCF-10-A as well (Fig. S26). Since, 10 μM concentration was used for the photophysical studies and has shown no considerable dark toxicity in both the normal and cancer cells, the same concentration was maintained for the time-dependent cellular internalization studies.

Important variables of the pharmacokinetic and pharmacodynamic characteristics of medicines and therapeutic candidates include successful cellular uptake and membrane permeability. The innate fluorescence property renders an added advantage of tracking the fate and activity of the molecule within the cell without the aid of a tracking reagent. Cellular internalization of our candidate molecule Ir-CN at three different time points (30 min, 60 min, and 120 min) was monitored by visualizing the fluorescence emitted from MCF-7 cells treated with it. Though the compound was seen successfully internalizing from 30 min of incubation onwards, maximum fluorescence intensity was observed with 60 min incubation, and no further increase was seen even with 120 min of incubation. Therefore, 60 min was fixed as the optimal time of internalization for further experiments (Fig. 3b, c). Besides, the concentration-dependent cellular internalization studies demonstrated that the probe fluorescence is visible even at a concentration of 5 μM but less intense as compared to 10 μM or 15 μM concentrations (Fig. 3d, f). Thus 10 μM concentration of Ir-CN for 60 min incubation was chosen for all the further experiments. With this optimized internalization time and concentration, Ir-CN uptake by MCF-7 cells was again confirmed using SERS analysis. Upon SERS imaging, Ir-CN specific peaks (1023 cm^{-1}, 2129 cm^{-1}) were observed from the average scan spectra of the treated cells (Fig. S18 a, b, c) as compared to the untreated control cells which only produced the cell peaks (Fig. S18 d, e, f).

2.6. Assessment of Mitochondria Targeting Ability of Ir-CN

MCF-7 cells were treated with Ir-CN with the optimized concentration of 10 μM followed by mitotracker green, lysotracker green, and nuclear targeting Hoechst as per the pre-optimized condition for colocalization experiment. The red fluorescence of Ir-CN and green fluorescence from the lyso and mitotrackers and blue fluorescence from Hoechst-33,342 were subjected to superimposition. Ir-CN was found to be superimposed well with the green fluorescence of the mitotracker as shown in Fig. 4a, with a Pearson coefficient value of 0.9, which predicates the fact that the probe is targeting mitochondria. In the case of the nuclear and lysotrackers, only 0.6 and 0.54 were obtained as their respective R values, indicating minimal targeting of the probe molecules towards those organelles (Fig. 4).

2.7. Assessment of the PDT Effects of Ir-CN in MCF-7 Cells

The excitation of the photosensitizers produces abundant amounts of singlet oxygen, a striking feature exploited in PDT. Numerous anticancer drugs are also known to generate singlet oxygen, which in turn

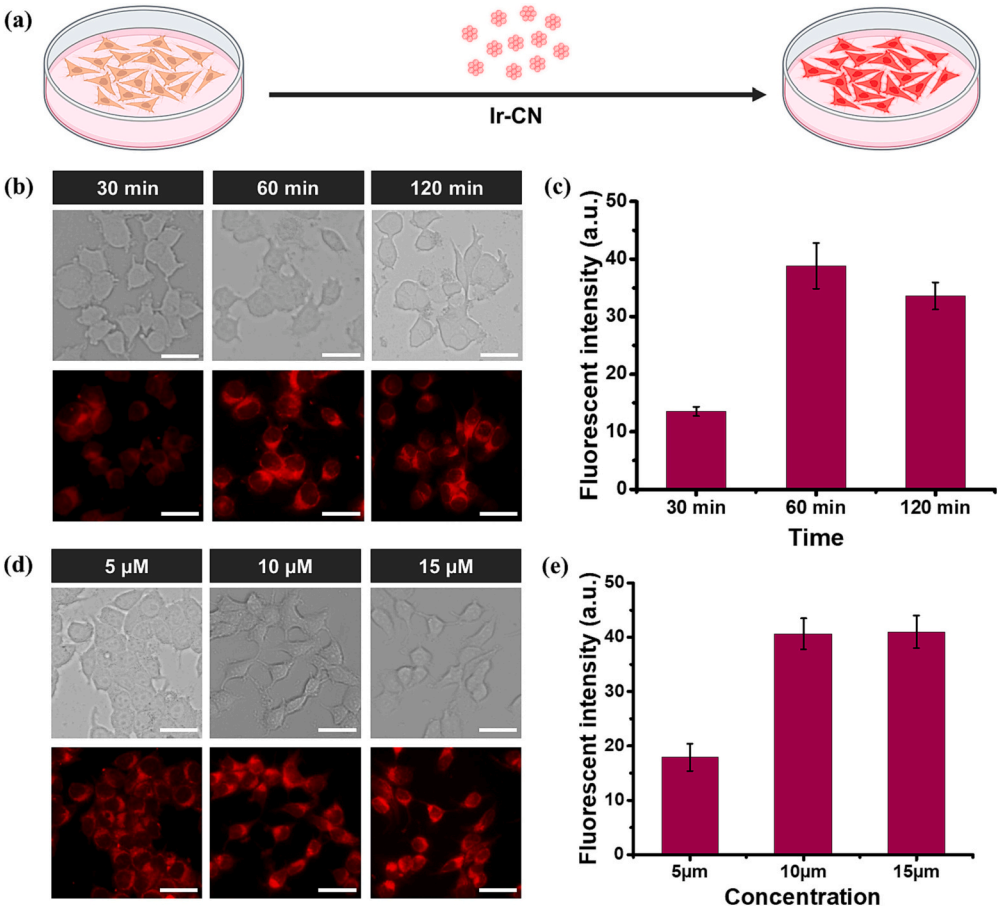

Fig. 3. (a) A pictorial representation of internalization of Ir-CN into MCF-7 cells. Standardization of concentration and duration of exposure to Ir-CN via (b) time-dependent cellular internalization studies (c) graph showing fluorescence intensity at different durations of incubation with the complex (d) concentration-dependent cellular internalization studies (e) graph depicting fluorescence intensity upon treatment with different concentrations of the complex. (scale bar = 50 μM).

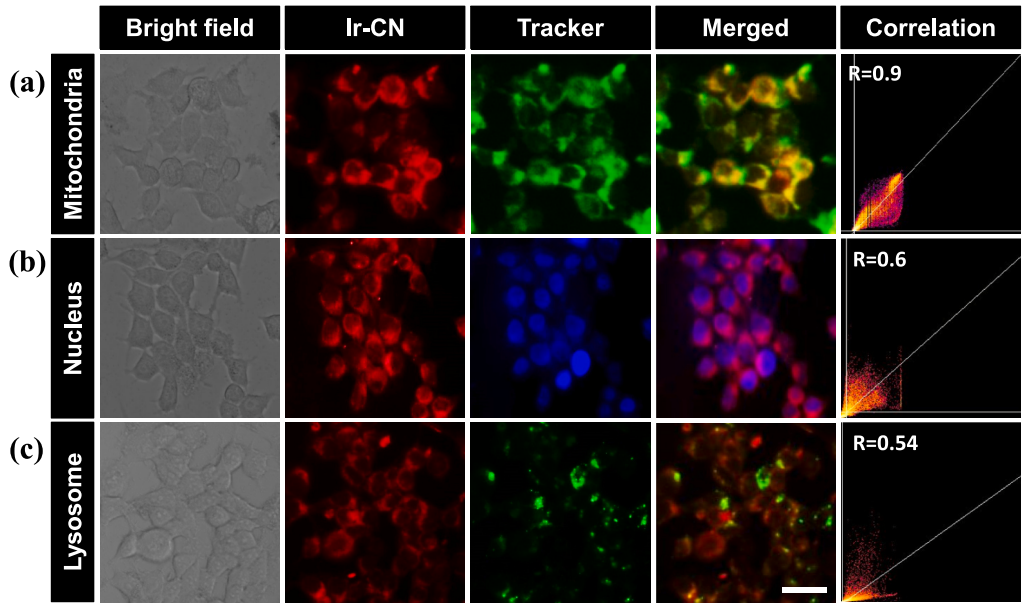

Fig. 4. Colocalization studies for the precise identification of the organelle to which Ir-CN is localized within the cell using (a) Mito tracker green, (b) Nuclear tracker (Hoechst) and (c) Lyso tracker green (Scale bar = 50 μm). (For interpretation of the references to colour in this figure legend, the reader is referred to the web version of this article.)

acts as "poison" towards the cells, causing significant depletion in cell viability. [31]

MTT assay performed with the Ir-CN treated, laser irradiated (405 nm) cells showed a profound cytotoxic effect with a cell death rate of 81%. Whereas, the Ir-CN-treated non-irradiated cells and untreated laser-exposed cells showed only about 10% and 3.9% cytotoxicity respectively. The cytotoxic response brought by Ir-CN PDT was found to be better than that of Doxorubicin-induced cytotoxicity at the same concentration of 10 μM within 24 h time (Fig. 5b). Thus, it is evident that laser irradiation activates the Ir-CN molecules internalized by the cells and triggers ROS-mediated cell death. The ROS generation was analyzed by fluorescent imaging and flow cytometric analysis using DCFH-DA staining assay [32] (Supporting information 3.4, Fig. S18).

2.8. Evaluation of Programmed Cell Death Phenomenon by Ir-CN

It is a well-known fact that irradiation of photosensitized cells leads to heightened light-catalyzed singlet oxygen generation in close proximity to the subcellular location of photosensitizer binding. The phototoxicity in the cells is predominantly mediated by the rapid initiation of apoptosis, a very complex, multi-step, multi-pathway cell-death process. Tumor cells exhibit the tendency to resist apoptotic progression and proliferate in an uncontrollable manner to facilitate cancer development. Thus, an approach of modulating key elements in the apoptotic pathway can be the righteous strategy for therapy-induced tumor-cell death [33]. The PDT-mediated singlet oxygen generation is reported to activate some proapoptotic proteins while inhibiting some anti-apoptotic signal cascades, ultimately leading to programmed cell death. As mitochondria is the powerhouse of the cell that controls redox homeostasis and apoptosis, mitochondria-targeting photosensitizers can be considered more effective candidates for photodynamic therapy [34]. Since Ir-CN is found to colocalize in the mitochondria, it enables mitochondria-mediated phototoxicity.

The apoptotic changes are manifested by chromatin condensation, membrane damage, exposure of phosphatidyl serine on the outer layer of the plasma membrane etc. Annexin V apoptotic assay was conducted to determine the percentage of cells in each phase of cell death like early apoptosis, late apoptosis, or necrosis. Here we employed Annexin V-FITC conjugate, which can specifically bind to the phosphatidyl serine expressed on the surface of the apoptotic cells to provide the green fluorescence of FITC. Co-staining with PI enabled the segregation of the cells in early apoptosis with more FITC fluorescence and less PI fluorescence (Q4) and late apoptotic cells with both FITC and PI fluorescence(Q2). Healthy cells are least stained by both dyes (Q3) while the necrotic cell population has the maximum PI fluorescence (Q1). Here we observed >50% of cells in the early apoptotic stage of Ir-CN + laser-treated cells meanwhile the probe-alone treated cells and untreated cells + laser groups showed only 4.7% and 10% cells in the same quadrant (Q4) respectively with the maximal distribution of the cells in healthy cell quadrant (Q3). A small population of cells in Ir-CN + laser-treated group was also found to be in a late apoptotic state as well, emphasizing the PDT-mediated apoptosis-inducing effect of Ir-CN (Fig. 5c and d).

Further, cell staining apoptotic assays were performed to conclude the cell death-inducing effect of Ir-CN-PDT. For this, Acridine orange-ethidium bromide dual staining was conducted to visualize orange-red fluorescing apoptotic cells. The assay exploits the ability of the dyes to cross the cell membrane. Acridine orange can diffuse into intact cell membranes and fluoresce green whereas ethidium bromide is able to cross only the compromised cell membranes such as those of necrotic or apoptotic cells [35,36]. Thus, the live cells, with acridine orange alone, fluoresce green while the dead cells and those with a compromised membrane fluoresce red due to ethidium bromide. Fig. 5e depicts the significant cell death brought by Ir-CN + laser treatment with the fluorescence of ethidium bromide, whereas the probe alone treated and control cells remain healthy mainly showing green fluorescence. A few dead cells were observed with the laser-exposed group (Ir-CN untreated), which was not significant as compared to Ir-CN + laser treatment group. Similar results were obtained with the APOP staining assay, where the dead cells take up the dye and hence be seen as pink-colored cells under the bright field of microscope due to the damaged cell membrane, while the healthy cells remain unstained (Fig. S21a). Maximum cell death was visible in the Ir-CN + laser-treated cells. Similar effects were manifested in trypan blue dye exclusion assay as well. Trypan blue is an acidic azo dye that is impermeable to the intact cell membrane. The dye will be taken up by the dead cells with damaged cell membranes so that the cytoplasm will be stained blue in colour [37]. The untreated control cells with and without laser exposure and Ir-CN alone treated groups mostly showed viable cells with clear cytoplasm

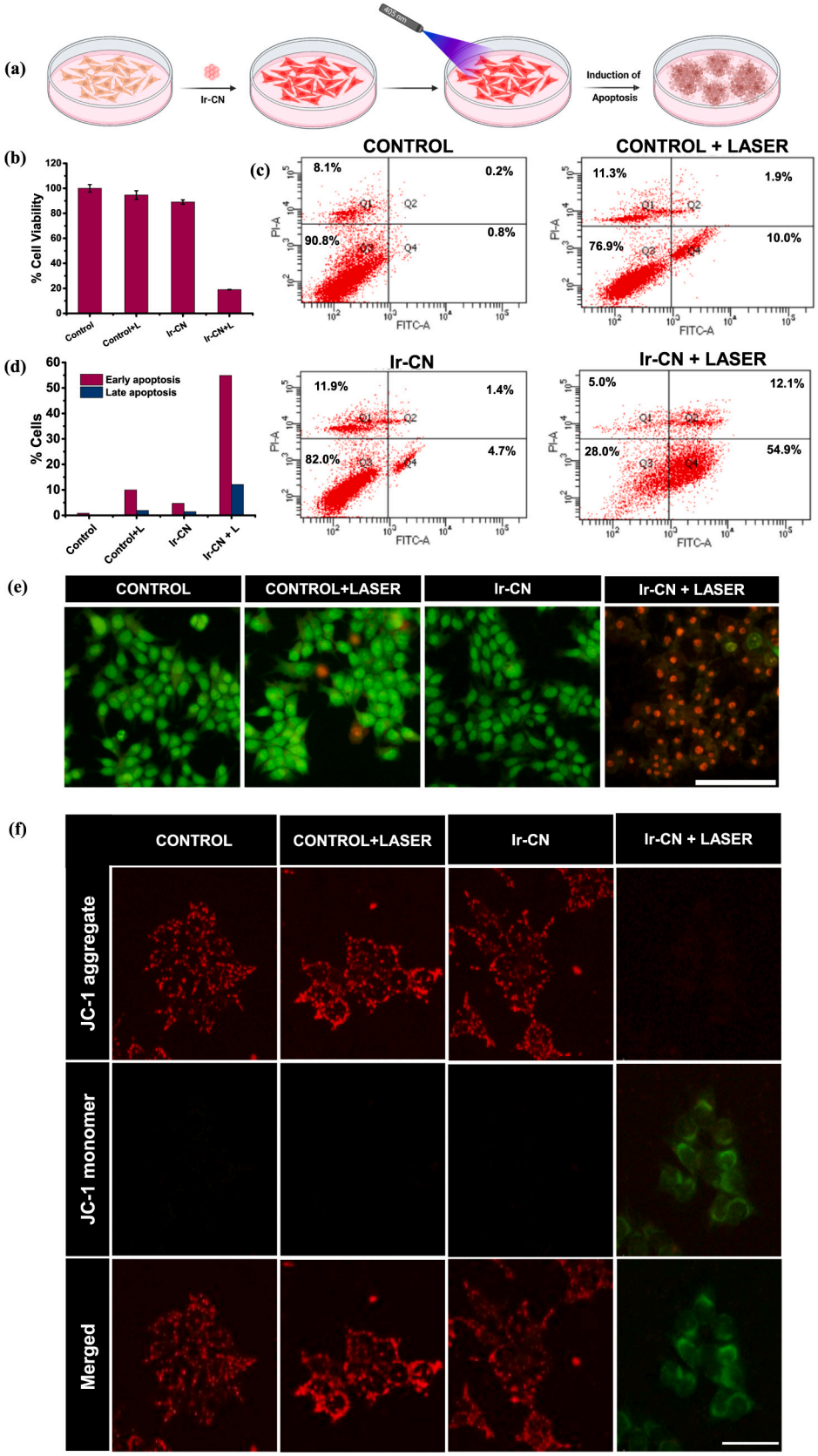

Fig. 5. (a) A pictorial representation of Ir-CN showing its PDT effect (b) a graph depicting the significant depletion of percentage cell viability when treated with Ir-CN and irradiated with laser, (c) Quantification of apoptosis by flow cytometry using Annexin V assay, and (d) graphical representation of its results (e) evaluation of apoptotic inductions through PDT by Ir-CN in MCF-7 cells acridine orange-ethidium bromide dual staining assay (live-dead assay) (scale bar = 100 μM) (f) JC-1 mitochondrial membrane potential assay (scale bar = 50 μM).

while the Ir-CN treated, laser-irradiated cells showed the maximum percentage of blue-colored dead cells (Fig. S21b).

Mitochondrial transmembrane potential ($\Delta\Psi_m$) can be considered as an essential parameter of mitochondrial function. Apoptosis is also known for its characteristic feature of a significant depletion in this potential due to enhanced membrane permeability and subsequent loss of electrochemical potential. The lipophilic, cationic dye JC-1 can enter and accumulate in the negatively charged mitochondria of healthy cells with a normal $\Delta\Psi_m$. It spontaneously forms reversible complexes (J aggregates) in a concentration-dependent manner with its excitation and emission in the red spectrum (maximum at ~590 nm), unlike its naturally green fluorescent monomer. In apoptotic cells, though the dye enters the mitochondria, JC-1 does not reach sufficient concentration to trigger the formation of J aggregate formation occurs only to a lesser degree due to a lesser negative environment, thus giving green fluorescence of the monomer. The reduction in the red-to-green fluorescence intensity ratio therefore indicates mitochondrial depolarization [38]. Since Ir-CN also exhibits red fluorescence, the experiment was carried out 24 h later for Ir-CN-containing wells, to allow the complex to have sufficient time to undergo metabolism, so that it does not interfere with the fluorescence of the JC-1 aggregate. As indicated in Fig. 5f the sufficient entry of the dye and thereby the J aggregate formation is found to be difficult in case of cells treated with Ir-CN and irradiated with laser, compared to others. The low aggregate: monomer ratio in such cells proves the reduction in the MMP achieved as a consequence of PDT-induced apoptosis by Ir-CN (Fig. S27).

Yet another hallmark of apoptotic cells, the phenomenon of nuclear condensation was also observable in the Ir-CN+ laser-treated cells with the staining of nuclear dye Hoechst 33342 (Fig. 6c) as compared to other treatment groups. Here, the nuclei of healthy cells will appear in a round shape with uniform staining whereas the apoptotic cell will have brighter and irregularly shaped nuclei. Together with this, internucleosomal degradation of double-stranded DNA by the action of caspase-activated DNase (CAD) on the genomic DNA is also an observable change associated with apoptosis. This leads to fragments of sizes in multiples of 180-200 bp, which when separated and visualized on an agarose gel electrophoresis, form a distinctive ladder pattern [39]. As in Fig. 6a, the typical laddering pattern of DNA fragments on the gel was observed in case of the Ir-CN treated, laser-irradiated sample, compared to the others. This also points towards the apoptosis-inducing effect of Ir-CN's PDT.

The SERS spectra of isolated DNA from each sample were recorded for the reconfirmation of the characteristic DNA fragmentation associated with apoptosis. As shown in Fig. 6b, several signature Raman peaks of DNA were obtained of which some show a significant shift or decrease in intensity in the case of DNA from the Ir-CN treated, laser-irradiated samples. The intensities of peaks at 766 cm^{-1}, 782 cm^{-1} and 877 cm^{-1} corresponding to the pyrimidine, DNA mode vibration and C-O-C vibration of sugar backbone respectively were found to be decreasing and disappearing in the case of Ir-CN treated, laser irradiated sample. Similar was the case of peaks at 1002 cm^{-1} (C-C aromatic ring vibration of N bases), 1085–1098 cm^{-1} phosphate backbone stretching, 1175 cm^{-1} Cytosine and Guanine,1304 cm^{-1} for Adenine and Cytosine, 1455⁻1460 & 1575 cm^{-1} for DNA bases ring breathing, nucleic acid mode and 1605 cm^{-1} Cytosine peaks. Whereas, 1620–1750 cm^{-1} peak for base pairing and H bond between N bases showed remarkable peak enhancement which may be due to the DNA Breakage and exposure of the double helical structure to the SERS substrate (Table S5).

Cell cycle arrest (CCA) is one of the prime candidates for effective cancer therapy and a characteristic of various therapeutic modalities [40]. Though the mechanism remains unclear, PDT is also reported to have a biological effect on CCA in cancer cells [41]. To accurately identify the phase of cell cycle being arrested as a part of the PDT by Ir-CN, a propidium iodide-based, flow cytometric analysis of the DNA content in the cells was done. Based on the DNA content in them, the percentage of cells in each of the phases (sub-G_0, G_1, S and G_2) were evaluated. As depicted in the graph (Fig. S22), control, compound treated and laser-treated cells showed a normal pattern of the cell cycle with its sub-G_0 population as insignificantly low as 0.5–0.6%, whereas Ir-CN treated laser irradiated cells showed not only a decrease of >20% of the cell population in G_1 phase but also a dramatic increase in those at its sub-G_0 phase to 27.3%. The sharp elevation in the sub-G_0 cell population clearly demonstrates the happening of apoptosis induced by the PDT effect of our compound (Fig. 6d).

Disruption and degradation of proteins, DNA, and other biomolecules that occur as a part of apoptosis show momentous changes in the Raman fingerprint patterns of the cells. Thus, Raman spectroscopy has been successfully implemented to track the apoptotic events in the cells. The Ir-CN treated and untreated cells were darted with laser, and their Raman spectra were recorded. Apoptotic behavior was expected only in the former group of cells. A decline in intensity of the peak at 838 cm^{-1} which corresponds to the breakage of the phosphodiester backbone of DNA resulting in the purine base exposure, was observed in the cells compound treated-laser shined cells, as compared to the other group. An increase in the peak intensity of the former sample at 1585 cm^{-1} could be assigned to the N_7-H vibration of guanine and adenine due to their exposure, clearly to DNA fragmentation. The C-H deformation of these bases are also evident from the heightening of the peak at 1400–1480 cm^{-1}. The disruption of protein tertiary structure and denaturation becomes apparent through the sharp hike observed in the peak at 1000 cm^{-1} in the former group of cells which is obviously suggestive of the exposure of hydrophobic amino acids such as phenylalanine, tryptophan and tyrosine due to the absence of secured positioning and protection within the intricately folded proteins [42,43] (Fig. 6e).

In the realm of apoptosis, Cytochrome c (Cyt c) unquestionably plays a leading role. It is resident of the mitochondrial intermembrane space and normally functions in the electron shuttle between complex III and IV. Cyt c is discharged into the cytosol as a result of apoptotic stimuli, where, it facilitates allosteric activation and formation of a hepta-oligomer with the adapter molecule Apaf-1 (apoptosis-protease activating factor-1), leading to apoptosome formation [44]. Here we have recorded the SERS spectra to track the spectral signature of cytochrome *c* which has been released in the initial stage of apoptosis. The Raman peaks characteristic of cytochrome *c* at 750 cm^{-1} and 1050 cm^{-1} [42] along with the other peaks corresponding to apoptosis were observed only from Ir-CN treated cells, after one and two hours of laser irradiation (Fig. 6f).

Further, to confirm the ROS generation that happened upon laser irradiation on Ir-CN treated cells, DCFDA staining was performed followed by flow cytometric analysis. As expected, the maximum ROS generation was found in the Ir-CN treated laser irradiated group as compared to the others (fig). By virtue of the PDT effect, disruption of respiratory chain and thereby a decline in the ATP level was also expected. To substantiate this claim, ATP determination assay was performed to estimate the amount of ATP generated in each group. The percentage of ATP was observed to fall below 25% in the case of the Ir-CN treated, laser-irradiated group as compared to the untreated control (Fig. 6h). This decrease in ATP level was found to be significantly different from control + laser treated as well as Ir-CN treated groups ($^{***}p < 0.001$) that further authenticate the claim.

3. Conclusions

In conclusion, our investigation focused on evaluating the phototherapeutic potential of two cyclometalated Iridium (III) molecular probes, Ir-CN and Ir-H, with a specific emphasis on mitochondria-mediated cell death. Through a comprehensive analysis, Ir-CN emerged as the preferred candidate for further investigation owing to its superior photosensitizing characteristics and a more favorable toxicity profile compared to Ir-H. The notable features of Ir-CN, including a substantial singlet oxygen quantum yield, were identified

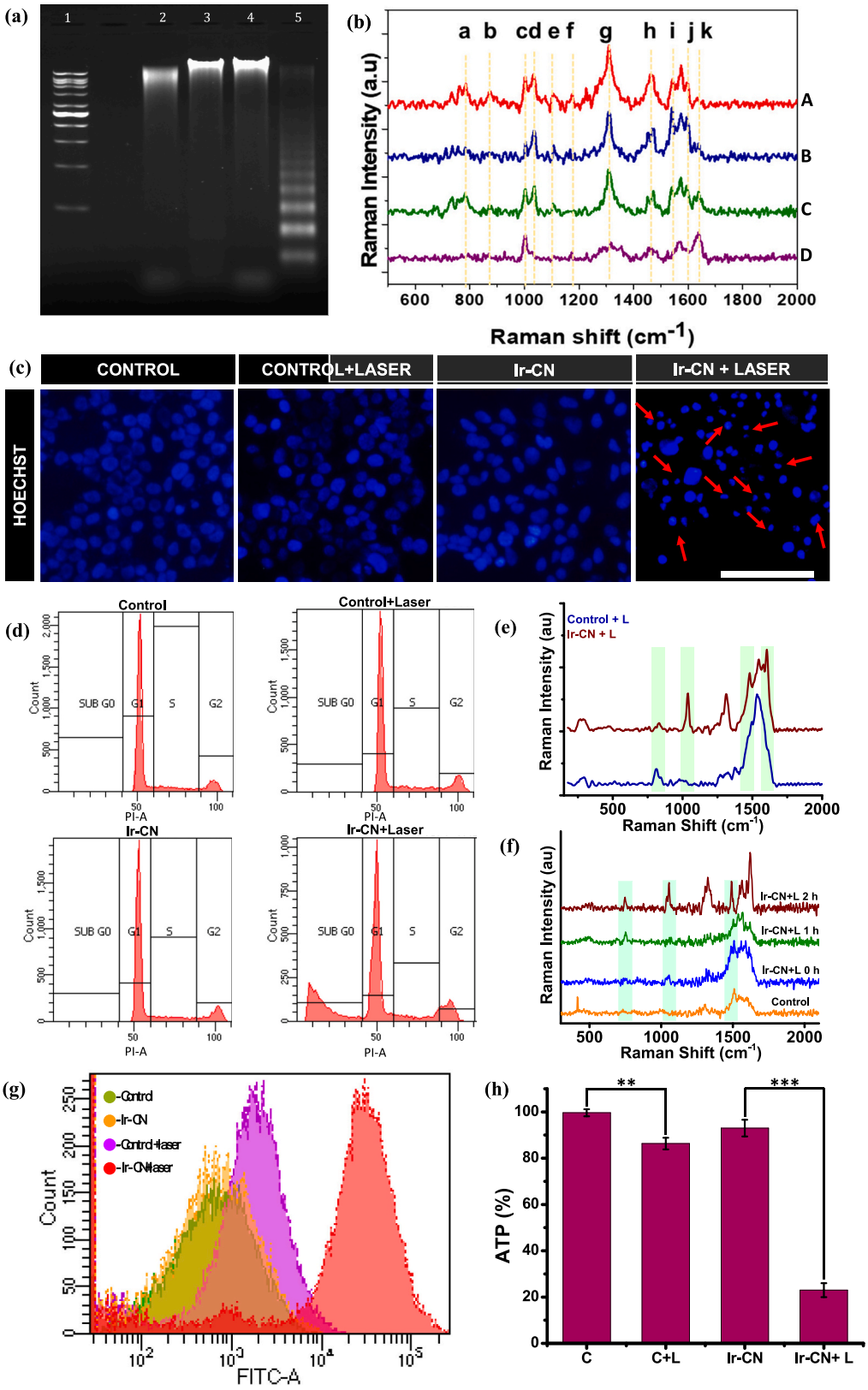

Fig. 6. Nuclear fragmentation and condensation induced by Ir-CN upon laser treatment proven with (a) DNA laddering by AGE (b) SERS analysis of DNA fragmentation (A- control, B- control+laser, C- Ir-CN, D- Ir-CN + laser), and (c) Hoescht nuclear staining showing heterochromatinization (scale bar = 100 μM) (d) Cell cycle analysis clearly showing G1 phase arrest (e) SERS spectra showing the peaks characteristic of apoptosis in Ir-CN treated laser darted cells (f) SERS spectra revealing Cyt C release occurred in the initial stages of apoptosis induced by the PDT effect of Ir-CN (g) ROS generation study using flow cytometric analysis

employing DCFDA staining method (h) Estimation of respiratory chain damage ATP determination assay (control vs control+laser- $^{**}P < 0.01$, Ir-CN vs Ir-CN + laser $^{***}P < 0.001$, control+laser vs Ir-CN + laser $^{***}P < 0.001$).

as pivotal attributes for its potential application as a photodynamic therapy (PDT) agent. The robust spin-orbit coupling associated with the central iridium metal played a key role in facilitating efficient singlet oxygen generation, enhancing the overall efficacy of Ir-CN in PDT. The pronounced red fluorescence emitted by Ir-CN not only allowed for effective visualization of its cellular uptake but also contributed to its targeted localization within mitochondria. The positive charge carried by the central metal atom in Ir-CN was instrumental in enhancing its affinity for mitochondria, enabling specific PDT effects within these cellular organelles. Experimental evidence supporting the induction of apoptosis by Ir-CN in MCF-7 cells was robust, as demonstrated through Annexin V-FITC assay, revealing a predominant apoptotic effect with a significant proportion of cells in the early apoptotic phase. This observation was further corroborated by monitoring the release of Cytochrome-C using Surface-Enhanced Raman Spectroscopy (SERS). Characteristics indicative of Ir-CN PDT-induced apoptosis, such as cell nuclear and membrane damage, DNA condensation, and protein degradation, were observed through fluorescence assays and SERS measurements. The DCFDA assay as well as the cellular ATP estimation confirmed the enhanced ROS generation and declined ATP levels due to Ir-CN PDT. Thus, the mechanism of apoptotic induction is supposed to be mediated via ROS-induced disruption of the electron transport chain causing energy deprivation in the cells. These findings collectively underscore the potential of Ir-CN as a PDT molecular probe with promising therapeutic benefits. The outcomes of this study pave the way for future clinical translation, offering a novel avenue for the development of targeted and effective phototherapeutic strategies in the realm of cancer treatment.

4. Materials and Methods

The chemicals including 4,4′-dibromo-2,2′-bipyridine, 4-cyanophenyl boronic acid, phenylboronic acid, potassium carbonate, Pd$(PPh_3)_4$, $IrCl_3{\cdot}xH_2O$, 2-phenyl pyridine, 2-methoxy ethanol, methyl iodide, diphenylisobenzofuran were purchased from TCI Chemicals and TBAB (Tetrabutylammonium bromide) was procured from Sigma Aldrich. All solvents were purchased from Merck and were of reagent grade. Standard procedures were followed for drying and distilling all solvents prior to use. All NMR spectra were recorded on a Bruker 500 MHz FT-NMR (model) spectrometer at 25 °C. The chemical shift (δ) data and coupling constant (J) values were given in parts per million (ppm) and Hertz (Hz), respectively. High-resolution mass spectra (HRMS) were recorded on a Thermo Scientific Exactive ESI-MS spectrophotometer. UV/Visible spectra were obtained by using a Shimadzu UV-2600 UV–Vis spectrophotometer and emission spectra were recorded on a Fluoromax-4 Spectrofluorometer with a 1 cm quartz cuvette. All experiments were carried out at 298 K unless otherwise specified. SERS experiments were performed using a WITec Raman microscope (WITec, Inc., Germany) containing 600 g/mm grating and Peltier cooled charge-coupled device detector unit. The samples were excited using a 633 nm laser with 10 mW power, and the Stoke-shifted Raman spectra were collected in the region of 300–2000 cm^{-1} with a resolution of 1 cm^{-1} and an integration time of 1 s and 10 accumulations. Prior to each measurement, calibration was done with a silicon standard (Raman peak at 520 cm^{-1}). WITec Project Plus (v 5.2) software package was employed for data processing.

In vitro, phototherapeutic potential, and all other imaging studies of Ir-CN were performed using MCF-7 cell line procured from ATCC. The cells were maintained in tissue culture flasks (T25 and T75) with Dulbecco's Modified Eagle Medium (DMEM, Sigma Aldrich) supplemented with 10% Fetal Bovine Serum (FBS, HiMedia), 1% antibiotic antimycotic solution (Anti-Anti 100×, Gibco). Flasks were incubated at 37 °C and 5% CO_2. The cells were sub-cultured upon attaining 80% confluency by trypsinization, after rinsing with PBS (Phosphate Buffered Saline, pH 7.4). Trypsin-EDTA solution 10× (0.5 Trypsin, 0.2% EDTA in 0.85% normal saline, Gibco) was used for detaching cells from the culture flask. All the cell images were captured using Nikon Eclipse TS100 with Nikon NIS Elements software unless mentioned. All OD measurements for biological studies were done using Synergy H1 microplate reader, Bio Tek Instruments, USA. All the flow cytometry and its data analysis were done using BD FACSAria™ II and BD FACSDiva™ software respectively.

The DNA is extracted from the cells using the genomic DNA extraction kit (Geneaid Blood/Cell DNA Mini Kit (GB100) and the purity of the DNA is estimated using nanodrop (Synergy H1, Biotek). The samples are made to undergo agarose gel electrophoresis (0.8% agarose). The laddering pattern on the gel is photographed using ChemiDoc imaging system (Bio-rad).

The following experiments were performed. The detailed methodology of each experiment is provided in the supporting information (SI).

4.1. Design and Synthesis of the Cyclometalated Ir(III) Complexes

The detailed steps of synthesis for the as-developed candidate cyclometalated iridium (III) complexes Ir-CN and Ir-H are given in the supporting information. The prepared complexes were well characterized through ^1H NMR, ^{13}C NMR, and HRMS spectroscopic techniques.

4.2. Photophysical and Stability Assessment of Ir-CN and Ir-H

The absorbance, emission, and Raman spectra of the compounds were recorded. The compound was exposed to long UV at 405 nm laser in order to assess the maximum duration of photostability. pH titration at several pH levels ranging from 4.5 to 9.5 was utilized to confirm the stability of compounds' absorption and emission characteristics in this range of pH environments.

4.3. Photooxidation and Singlet Oxygen Generation Studies of Ir-CN and Ir-H

Using the well-known $^1O_2$ scavenger dye 1,3-diphenylisobenzofuran (DPBF) (Fig. 2c) and a structurally significant molecule $[Ru(Bpy)_3]Cl_2$ as standard reference material, the Ir-CN was examined for its ability to generate $^1O_2$. The singlet oxygen production in the solution state was further confirmed by the well-known singlet oxygen indicator Singlet Oxygen Sensor Green (SOSG).

4.4. Evaluation of Cytotoxicity and Cellular Internalization of Ir-CN and Ir-H

MTT assay was used to determine the extent of dark toxicity rendered by the complexes. Based on the results of the MTT assay, the better candidate was chosen and its time and concentration-dependent internalization studies were conducted.

4.5. Assessment of Mitochondrial Targetability of Ir-CN

Even though it was hypothesized that by virtue of the positive charge of the complex would specifically move to the mitochondria, colocalization studies using mito, lyso, and nuclear trackers were conducted to specifically identify the organelle to which the complex is localized within the cell.

4.6. Assessment of the PDT Effects of Ir-CN on MCF-7 Cells

MTT assay was performed on Ir-CN treated, laser (405 nm) irradiated

cells to estimate the cytotoxicity caused upon treatment. The generation efficiency of reactive oxygen species as a part of the PDT effect of the compound was also confirmed by the DCFDA assay by fluorescent imaging and flow cytometric analysis as detailed in the supporting information.

4.7. Evaluation of Programmed Cell Death Phenomenon by Ir-CN-Induced PDT

Basic staining assays such as live-dead assay, trypan blue assay, APOP assay, and Hoechst staining along with Annexin V-FITC assay, DNA laddering, and JC-1 assay were performed for the evaluation of apoptosis induced by PDT effect exerted by the complex. The cell cycle analysis was also performed on the cells. Raman spectroscopy was also employed for the detection of cytochrome *c* release and all other apoptotic changes happening as a part of PDT. The extent of mitochondrial respiratory chain damage was estimated by intracellular ATP determination assay.

Author Contributions

The manuscript was written through the contributions of all authors. All authors have given approval to the final version of the manuscript.

CRediT authorship contribution statement

Chandana Reghukumar: Writing – review & editing, Writing – original draft, Validation, Methodology, Investigation, Formal analysis, Data curation, Conceptualization. **Shanmughan Shamjith:** Writing – review & editing, Validation, Software, Formal analysis, Data curation. **Vishnu Priya Murali:** Writing – review & editing, Visualization, Validation, Software, Formal analysis, Data curation. **Pilankatta K. Ramya:** Software, Data curation. **Kokkuvayil Vasu Radhakrishnan:** Supervision, Funding acquisition. **Kaustabh Kumar Maiti:** Writing – review & editing, Supervision, Resources, Project administration, Funding acquisition, Conceptualization.

Declaration of Competing Interest

The authors declare that they have no known competing financial interests or personal relationships that could have appeared to influence the work reported in this paper.

Data availability

No data was used for the research described in the article.

Acknowledgments

K.K.M. and K.V.R. thanks, CSIR and ICMR (project no. 5/4-5/3/01/DHR/NEURO/2020-NCD-I), Government of India for funding. V.P.M. thanks ICMR-DHR, Government of India for the Young Scientist fellowship (R.12014/22/2021-HR/*E*-office:8114716). The support rendered by Dr. C. H. Suresh, Chief scientist, CSTD, CSIR-NIIST for the computational studies of the synthesized molecular probes is also acknowledged.

AcSIR Ph.D. students C.R., S.J.S, and P.K.R. acknowledge ICMR, UGC, and CSIR respectively for their research fellowships. Thanks to all K. K. M. group members for their support.

Appendix A. Supplementary Data

Supplementary data to this article can be found online at https://doi.org/10.1016/j.jphotobiol.2023.112832.

References

[1] J. Rak, Cancer: organ-seeking vesicles, Nature. (2015) 10–11, https://doi.org/10.1038/nature15642.
[2] D. Hanahan, R.A. Weinberg, Hallmarks of cancer: the next generation, Cell. 144 (2011) 646–674, https://doi.org/10.1016/j.cell.2011.02.013.
[3] S.Y. Kim, Cancer energy metabolism: shutting power off cancer factory, Biomol. Ther. (Seoul). 26 (2018) 39–44, https://doi.org/10.4062/biomolther.2017.184.
[4] B.a. Chabner, T.G. Roberts, Timeline: chemotherapy and the war on cancer, Nat. Rev. Cancer 5 (2005) 65–72, https://doi.org/10.1038/nrc1529.
[5] D.E.J.G.J. Dolmans, D. Fukumura, R.K. Jain, Photodynamic therapy for cancer, Nat. Rev. Cancer (2003), https://doi.org/10.1038/nrc1071.
[6] D. Zhang, M. Wu, Y. Zeng, L. Wu, Q. Wang, X. Han, X. Liu, J. Liu, Chlorin e6 conjugated poly(dopamine) nanospheres as PDT/PTT dual-modal therapeutic agents for enhanced cancer therapy, ACS Appl. Mater. Interfaces 7 (2015) 8176–8187, https://doi.org/10.1021/acsami.5b01027.
[7] D.L. Sai, J. Lee, D.L. Nguyen, Y.-P. Kim, Tailoring photosensitive ROS for advanced photodynamic therapy, Exp. Mol. Med. 53 (2021) 495–504, https://doi.org/10.1038/s12276-021-00599-7.
[8] H. Huang, B. Yu, P. Zhang, J. Huang, Y. Chen, G. Gasser, L. Ji, H. Chao, Highly charged ruthenium(II) polypyridyl complexes as lysosome-localized photosensitizers for two-photon photodynamic therapy, Angew. Chem. 127 (2015) 14255–14258, https://doi.org/10.1002/ange.201507800.
[9] J.C.S. Simões, S. Sarpaki, P. Papadimitroulas, B. Therrien, G. Loudos, Conjugated photosensitizers for imaging and PDT in cancer research, J. Med. Chem. 63 (2020) 14119–14150, https://doi.org/10.1021/acs.jmedchem.0c00047.
[10] Y. Wu, J. Wu, W.Y. Wong, A new near-infrared phosphorescent iridium(iii) complex conjugated to a xanthene dye for mitochondria-targeted photodynamic therapy, Biomater. Sci. 9 (2021) 4843–4853, https://doi.org/10.1039/d1bm00128k.
[11] U. Ndagi, N. Mhlongo, M. Soliman, Metal complexes in cancer therapy – an update from drug design perspective, Drug Des. Devel. Ther. Volume11 (2017) 599–616, https://doi.org/10.2147/DDDT.S119488.
[12] Y.-J. Cho, S.-Y. Kim, C.M. Choi, N.J. Kim, C.H. Kim, D.W. Cho, H.-J. Son, C. Pac, S. O. Kang, Photophysics and excited-state properties of cyclometalated iridium(III)–platinum(II) and iridium(III)–iridium(III) bimetallic complexes bridged by dipyridylpyrazine, Inorg. Chem. 56 (2017) 5305–5315, https://doi.org/10.1021/acs.inorgchem.7b00384.
[13] Y. Wu, S. Li, Y. Chen, W. He, Z. Guo, Recent advances in noble metal complex based photodynamic therapy, Chem. Sci. 13 (2022) 5085–5106, https://doi.org/10.1039/D1SC05478C.
[14] S. Banerjee, A.R. Chakravarty, Metal complexes of curcumin for cellular imaging, targeting, and photoinduced anticancer activity, Acc. Chem. Res. 48 (2015) 2075–2083, https://doi.org/10.1021/acs.accounts.5b00127.
[15] O.J. Stacey, S.J.A. Pope, New avenues in the design and potential application of metal complexes for photodynamic therapy, RSC Adv. 3 (2013) 25550–25564, https://doi.org/10.1039/c3ra45219k.
[16] S. Shamjith, M.M. Joseph, V.P. Murali, G.S. Remya, J.B. Nair, C.H. Suresh, K. K. Maiti, NADH-depletion triggered energy shutting with cyclometalated iridium (III) complex enabled bimodal luminescence-SERS sensing and photodynamic therapy, Biosens. Bioelectron. 204 (2022), https://doi.org/10.1016/j.bios.2022.114087.
[17] X. Cai, K.N. Wang, W. Ma, Y. Yang, G. Chen, H. Fu, C. Cui, Z. Yu, X. Wang, Multifunctional AIE iridium (III) photosensitizer nanoparticles for two-photon-activated imaging and mitochondria targeting photodynamic therapy, J. Nanobiotechnol. 19 (2021), https://doi.org/10.1186/s12951-021-01001-4.
[18] B. Kar, U. Das, N. Roy, P. Paira, Recent advances on organelle specific Ru(II)/Ir (III)/Re(I) based complexes for photodynamic therapy, Coord. Chem. Rev. 474 (2023), https://doi.org/10.1016/j.ccr.2022.214860.
[19] Z. Li, Q. Gao, Induction of apoptosis in HT-29 cells by quercetin through mitochondria-mediated apoptotic pathway, Anim. Cells Syst. (Seoul). 17 (2013) 147–153, https://doi.org/10.1080/19768354.2013.793210.
[20] J.S. Arya, M.M. Joseph, D.R. Sherin, J.B. Nair, T.K. Manojkumar, K.K. Maiti, Exploring mitochondria-mediated intrinsic apoptosis by new phytochemical entities: an explicit observation of cytochrome *c* dynamics on lung and melanoma cancer cells, J. Med. Chem. 62 (2019) 8311–8329, https://doi.org/10.1021/acs.jmedchem.9b01098.
[21] M.D. Yaqoob, L. Xu, C. Li, M.M.L. Leong, D.D. Xu, Targeting mitochondria for cancer photodynamic therapy, Photodiagnosis Photodyn. Ther. 38 (2022), 102830, https://doi.org/10.1016/j.pdpdt.2022.102830.
[22] S. Heinz, A. Freyberger, B. Lawrenz, L. Schladt, G. Schmuck, H. Ellinger-Ziegelbauer, Mechanistic investigations of the mitochondrial complex I inhibitor rotenone in the context of pharmacological and safety evaluation, Sci. Rep. 7 (2017) 45465, https://doi.org/10.1038/srep45465.
[23] The 150 most important questions in cancer research and clinical oncology series: questions 94–101, Cancer Commun. 38 (2018) 69, https://doi.org/10.1186/s40880-018-0341-9.
[24] J.-J. Cao, C.-P. Tan, M.-H. Chen, N. Wu, D.-Y. Yao, X.-G. Liu, L.-N. Ji, Z.-W. Mao, Targeting cancer cell metabolism with mitochondria-immobilized phosphorescent cyclometalated iridium(III) complexes, Chem. Sci. 8 (2017) 631–640, https://doi.org/10.1039/C6SC02901A.
[25] H. Li, S.K. Kolluri, J. Gu, M.I. Dawson, X. Cao, P.D. Hobbs, B. Lin, G. Chen, J. Lu, F. Lin, Z. Xie, J.A. Fontana, J.C. Reed, X. Zhang, Cytochrome c release and apoptosis induced by mitochondrial targeting of nuclear orphan receptor TR3, Science 289 (2000) (1979) 1159–1164, https://doi.org/10.1126/science.289.5482.1159.

[26] H. Lu, X. Jiang, Y. Chen, K. Peng, Y. Huang, H. Zhao, Q. Chen, F. Lv, L. Liu, S. Wang, Y. Ma, Cyclometalated iridium(III) complex nanoparticles for mitochondria-targeted photodynamic therapy, Nanoscale. 12 (2020) 14061–14067, https://doi.org/10.1039/D0NR03398G.
[27] W. Lv, Z. Zhang, K.Y. Zhang, H. Yang, S. Liu, A. Xu, S. Guo, Q. Zhao, W. Huang, A mitochondria-targeted photosensitizer showing improved photodynamic therapy effects under hypoxia, Angew. Chem. Int. Ed. 55 (2016) 9947–9951, https://doi.org/10.1002/anie.201604130.
[28] M. Shao, M. Yao, X. Liu, C. Gao, W. Liu, J. Guo, J. Zong, X. Sun, Z. Liu, In vitro and in vivo of triphenylamine-appended fluorescent half-sandwich iridium(III) thiosemicarbazones antitumor complexes, Inorg. Chem. 60 (2021) 17063–17073, https://doi.org/10.1021/acs.inorgchem.1c02250.
[29] K.V. Sudheesh, P.S. Jayaram, A. Samanta, K.S. Bejoymohandas, R.S. Jayasree, A. Ajayaghosh, A cyclometalated Ir^{III} complex as a lysosome-targeted photodynamic therapeutic agent for integrated imaging and therapy in cancer cells, Chem. A Eur. J. 24 (2018) 10999–11007, https://doi.org/10.1002/chem.201801918.
[30] Z. Liu, W. He, Z. Guo, Metal coordination in photoluminescent sensing, Chem. Soc. Rev. 42 (2013) 1568, https://doi.org/10.1039/c2cs35363f.
[31] L.J. Schiff, W.C. Eisenberg, J. Dziuba, K. Taylor, S.J. Moore, Cytotoxic effects of singlet oxygen, Environ. Health Perspect. 76 (1987) 199–203, https://doi.org/10.1289/ehp.8776199.
[32] K. Pal, S. Roy, P.K. Parida, A. Dutta, S. Bardhan, S. Das, K. Jana, P. Karmakar, Folic acid conjugated curcumin loaded biopolymeric gum acacia microsphere for triple negative breast cancer therapy in invitro and invivo model, Mater. Sci. Eng. C 95 (2019) 204–216, https://doi.org/10.1016/j.msec.2018.10.071.
[33] B.A. Carneiro, W.S. El-Deiry, Targeting apoptosis in cancer therapy, Nat. Rev. Clin. Oncol. 17 (2020) 395–417, https://doi.org/10.1038/s41571-020-0341-y.
[34] P. Mroz, A. Yaroslavsky, G.B. Kharkwal, M.R. Hamblin, Cell death pathways in photodynamic therapy of cancer, Cancers (Basel). 3 (2011) 2516–2539, https://doi.org/10.3390/cancers3022516.
[35] A. Valsan, M.T. Meenu, V.P. Murali, B. Malgija, A.G. Joseph, P. Nisha, K. V. Radhakrishnan, K.K. Maiti, Exploration of phaeanthine: a bisbenzylisoquinoline alkaloid induces anticancer effect in cervical cancer cells involving mitochondria-mediated apoptosis, ACS Omega 8 (2023) 14799–14813, https://doi.org/10.1021/acsomega.3c01023.
[36] M.M. Joseph, A.N. Ramya, V.M. Vijayan, J.B. Nair, B.T. Bastian, R.K. Pillai, S. T. Therakathinal, K.K. Maiti, Targeted theranostic nano vehicle endorsed with self-destruction and immunostimulatory features to circumvent drug resistance and wipe-out tumor reinitiating cancer stem cells, Small. 16 (2020), https://doi.org/10.1002/smll.202003309.
[37] W. Strober, Trypan blue exclusion test of cell viability, Curr. Protoc. Immunol. 111 (2015), https://doi.org/10.1002/0471142735.ima03bs111.
[38] F. Sivandzade, A. Bhalerao, L. Cucullo, Analysis of the mitochondrial membrane potential using the cationic JC-1 dye as a sensitive fluorescent probe, Bio-Protoc. 9 (2019), https://doi.org/10.21769/BioProtoc.3128.
[39] B. Harshitha, B. Subhada, M. Mustafa, H. Solanki, N.M. Safiya, R.C. Tiwari, DNA laddering to evaluate cytogenetic damage in patients with periodontitis, J. Int. Soc. Prev. Commun. Dent. 9 (2019) 486, https://doi.org/10.4103/jispcd.JISPCD_245_19.
[40] M.G.S. Aithal, N. Rajeswari, Bacoside a induced sub-G0 arrest and early apoptosis in human glioblastoma cell line U-87 MG through notch signaling pathway, Brain Tumor Res. Treat. 7 (2019) 25, https://doi.org/10.14791/btrt.2019.7.e21.
[41] K. Moloudi, H. Abrahamse, B.P. George, Photodynamic therapy induced cell cycle arrest and cancer cell synchronization: review, Front. Oncol. 13 (2023), https://doi.org/10.3389/fonc.2023.1225694.
[42] J.B. Nair, M.M. Joseph, J.S. Arya, P. Sreedevi, P.T. Sujai, K.K. Maiti, Elucidating a thermoresponsive multimodal photo-chemotherapeutic nanodelivery vehicle to overcome the barriers of doxorubicin therapy, ACS Appl. Mater. Interfaces 12 (2020) 43365–43379, https://doi.org/10.1021/acsami.0c08762.
[43] B. Kang, L.A. Austin, M.A. El-Sayed, Observing real-time molecular event dynamics of apoptosis in living cancer cells using nuclear-targeted plasmonically enhanced Raman nanoprobes, ACS Nano 8 (2014) 4883–4892, https://doi.org/10.1021/nn500840x.
[44] C. Garrido, L. Galluzzi, M. Brunet, P.E. Puig, C. Didelot, G. Kroemer, Mechanisms of cytochrome c release from mitochondria, Cell Death Differ. 13 (2006) 1423–1433, https://doi.org/10.1038/sj.cdd.4401950.